GLAcier Feature Tracking testkit (GLAFT): A statistically and physically based framework for evaluating glacier velocity products derived from optical satellite image feature tracking

Whyjay Zheng[1,2], Shashank Bhushan[3], Maximillian Van Wyk De Vries[4,5,6], William Kochtitzky[7,8], David Shean[3], Luke Copland[7], Christine Dow[9], Renette Jones-Ivey[10], and Fernando Pérez[1]

[1]University of California Berkeley, Department of Statistics, Berkeley, CA 94720, USA
[2]National Central University, Center for Space and Remote Sensing Research, Zhongli, Taoyuan 320317, Taiwan
[3]University of Washington, Department of Civil & Environmental Engineering, Seattle, WA 98195, USA
[4]Saint Anthony Falls Laboratory, University of Minnesota, Minneapolis, MN, USA
[5]School of Environmental Sciences, University of Liverpool, Liverpool, L3 5DA, UK
[6]School of Geography and the Environment, University of Oxford, Oxford, OX1 3QY, UK
[7]Department of Geography, Environment and Geomatics, University of Ottawa, Ottawa K1N 6N5, Canada
[8]School of Marine and Environmental Programs, University of New England, Biddeford, ME 04005, USA
[9]Department of Geography and Environmental Management, University of Waterloo, Waterloo N2L 3G1, Canada
[10]University at Buffalo, Institute for Artificial Intelligence and Data Science, Buffalo, NY 14260, USA

Correspondence: Whyjay Zheng (whyjayzheng@gmail.com)

Abstract. Glacier velocity measurements are essential to understand ice flow mechanics, monitor natural hazards, and make accurate projections of future sea-level rise. Despite these important applications, the method most commonly used to derive glacier velocity maps, feature tracking, relies on empirical parameter choices that rarely account for glacier physics or uncertainty. Here we test two statistics- and physics-based metrics to ~~assess~~evaluate velocity maps derived from optical
5 satellite images of ~~at~~ Kaskawulsh Glacier, Yukon, Canada using a range of existing feature-tracking workflows. Based on inter-comparisons with ground-truth data, velocity maps with metrics falling within our recommended ranges contain fewer erroneous measurements and more spatially correlated noise than velocity maps with metrics that deviate from those ranges. Thus, these metric ranges are suitable for refining feature-tracking workflows and evaluating the resulting velocity products. We have released an open-source software package for computing and visualizing these metrics, the GLAcier Feature Tracking
10 testkit (GLAFT).

1 Introduction

Accurate measurements of glacier surface velocity are fundamental to answering some of the most societally relevant issues in the cryospheric sciences. Glacier flow speeds underpin many projections of future sea level rise (Moon et al., 2012; Mouginot et al., 2019; Shepherd et al., 2020), and they are essential for models used to understand the processes that control ice sheet
15 behavior – ice creep, basal sliding, and ice-ocean interactions (Holland et al., 2008; Burgess et al., 2013; Sundal et al., 2013; Zheng, 2022; Van Wyk de Vries et al., 2022). As a sensitive indicator of change, glacier velocities can be used to understand

and monitor dangerous glacier surges and detachments (Evans et al., 2009; Shangguan et al., 2021; Van Wyk de Vries et al., 2022), and quantify freshwater storage volumes in regions reliant on glacier melt as a water resource (Millan et al., 2022; Van Wyk de Vries et al., 2022). In each of these cases, accurate maps of ice velocity with rigorous uncertainty propagation

20 are needed to quantify the total uncertainty envelope of high-impact projections of future change. However, current methods for assessing ice-velocity map quality and uncertainty vary in different workflows, and are commonly derived from arbitrary thresholds or measurements over ice-free areas. The workflows and processing software may be easy to use, but the quality assessments for the resulting velocity maps, despite their many applications, rely on researchers who specialize in glacier dynamics. This technical limitation discourages other research and education communities from using glacier velocity data or

25 creates other concerns, such as a risk of over-interpretation during a time-sensitive hazard event.

The most widely used method for deriving glacier velocity at regional or global scales is feature tracking, which is also known as offset tracking, pixel tracking, speckle tracking, template matching, and particle image velocimetry ~~in fluid mechanics~~ (Bindschadler and Scambos, 1991; Strozzi et al., 2002; Moon et al., 2012; Dehecq et al., 2015; Fahnestock et al., 2016; Friedl et al., 2021). This technique tracks the movement of coherent patterns on the glacier surface (e.g., crevasses, medial moraines,

30 or other optical patterns or radar scatterers) between two satellite image acquisitions. To compute feature displacement, a 2D cross-correlation algorithm is used to prepare a correlation score "surface" for small image chips from the two images. The position of the highest peak in this correlation score surface then corresponds, in an ideal scenario, to the feature displacement between two images. Finally, this process is repeated for each image chip, producing the spatially continuous displacement field, ~~as the velocity map.~~which is used to prepare the velocity map with appropriate scaling based on the pixel dimensions and

35 time offset.

Both optical and synthetic aperture radar (SAR) images with a wide range of specifications are suitable for deriving feature-tracked ice velocity, as evidenced by applications using numerous earth-observing satellite data sets (e.g., Armstrong et al., 2016; Strozzi et al., 2017; Van Wychen et al., 2018; Altena et al., 2019; Millan et al., 2019). To date, all of the publicly available ice velocity datasets with a global extent have been created using feature tracking (Gardner et al., 2019; Friedl et al., 2021;

40 Millan et al., 2022). Despite its popularity, the feature tracking technique faces challenges ~~of~~involving optimization and ease of use. A feature_-tracking workflow contains several adjustable parameters and options, such as image preprocessing methods (typically high-pass or edge filters) and interpolation methods to locate a correlation peak with high precision. Researchers have explored this parameter space, offered recommended settings (Heid and Kääb, 2012; Fahnestock et al., 2016), and released public data sets with extensive documentation such as the NASA ITS_LIVE project (Gardner et al., 2019; Lei et al., 2022).

45 Still, the full parameter space has not been quantitatively studied for a range of different ice flow conditions. Several challenges prohibit further optimization. First, there is no benchmarking test suitable for inter-comparing velocity maps generated with different software packages and parameters. Second, it is challenging to validate the derived velocity maps due to a lack of contemporaneous in situ and satellite observations (Paul et al., 2017).

To lower the threshold of using and assessing feature-tracked glacier velocity maps for various applications, we set out to

50 develop new methods and create a user-friendly, open-source package that can be used to prepare, evaluate and improve glacier velocity products for a range of science applications. We present the GLAcier Feature Tracking testkit (GLAFT) package,

which can easily benchmark the quality of ice velocity maps using two statistics- and physics-based metrics ~~(Section 2)~~. The first metric identifies correct feature matches over static ground surfaces and their uncertainty. The second metric analyzes the velocity spatial coherence ~~of glacier flow~~ and evaluates how much the strain rate field reflects the ice flow dynamics.

To demonstrate how the metrics indicate the quality of ice velocity measurements, we use different parameter settings of various software packages to derive ~~processed~~ 172 glacier velocity maps for Kaskawulsh Glacier, Canada, from two Landsat 8 and two Sentinel-2 image pairs (Section 3.1.1). To evaluate these metrics, the derived velocity maps are compared with simultaneous in situ Global Navigation Satellite System (GNSS) data (Section 3.1.2), velocity products from the ITS_LIVE project (Section 3.1.3), and a feature-tracking map with an arbitrary, synthetic velocity field (Section 3.1.4). Finally, we review current approaches for estimating ~~flow speed~~ uncertainty and suggest a new framework for quality assessment of derived glacier velocity maps.

2   Defining good performance for glacier feature tracking

To evaluate the success of velocity maps derived from pairs of satellite images, it is necessary to identify the uncertainty of the feature-tracking algorithm used to create them. Since each velocity measurement is derived from the peak location of the cross-correlation surface (in units of pixels along two image axes), the primary source of error depends on the significance of the peak. If the correlation peak has a high signal-to-noise ratio (SNR), we can reasonably assume that the algorithm has found the correct match (i.e., the algorithm identified the same feature in both input images). In this instance, the uncertainty of the resulting pixel offset values (used to derive velocity) is determined by several factors, including the resolution of the input images, uncertainty of image co-registration (Kääb et al., 2016), shape of the correlation peak (Altena et al., 2022), and sub-pixel resampling errors (Sciacchitano, 2019). Based on simulations, the aggregated inherited uncertainty (2-sigma) for correct matches falls between 0.02 and 0.4 pixels (Sciacchitano, 2019). On the other hand, if the correlation peak is absent, has a low signal-to-noise ratio, or appears more than once on the correlation surface, the peak-finding algorithm can return an incorrect local maximum, producing an incorrect match and a biased velocity measurement.

Since SNR correlates to the matching correctness and provides a good pixel-based quality assessment, many feature tracking tools generate a SNR map as part of the standard output along with the velocity grid, such as CARST (Zheng et al., 2019, 2021) and GIV (Van Wyk de Vries and Wickert, 2021). Ideally, we want to exclude incorrect matches so that biased measurements do not affect the propagated uncertainty of ~~from propagating to~~ the derived velocity map ~~and calculate uncertainties for correct matches~~. Some published algorithms mask these pixels based on a threshold of SNR (Willis et al., 2012; Dehecq et al., 2015), while others use local coherence (Heid and Kääb, 2012; Lei et al., 2021) or absolute velocity thresholds (Heid and Kääb, 2012) to identify and remove incorrect matches. However, it may be impossible to identify all incorrect matches due to limited a priori knowledge of correct velocity ranges and a lack of ground truth data. Even with a carefully designed mask applied, both correct and incorrect matches are still likely to be present in the velocity map (e.g., Figure 3 in Heid and Kääb, 2012). As a result, the estimated a posteriori uncertainty (2-sigma) of the best-filtered feature displacement map is usually about 0.6 to 1.0 pixels (Strozzi et al., 2017; Zheng et al., 2019), ~~about~~ 2–3x larger than the theoretical ~~inherited~~ uncertainty.

In this study we designed ~~the evaluation metrics~~global (i.e., image-wide) metrics by considering the arguments above and the computational efficiency, flexibility, and compatibility for existing and emerging workflows that use advanced tracking techniques, such as Altena and Kääb (2020). ~~These metrics should provide a global (i.e., image-wide) estimate and~~Along with relevant qualitative assessments (e.g., spatial distribution of incorrect matches), ~~to~~these metrics evaluate how incorrect matches and variation of correct matches alter the true glacier velocity indicated by ice flow physics.

2.1 Metric 1: velocity measurements over static terrain

The first metric is rooted in a traditional approach for calibrating and estimating uncertainty of feature-tracked ice velocity. The central idea is to assume that adjacent ice-free terrain is static without horizontal or vertical movement, implying that any non-zero velocity values in these locations are measurement errors. ~~For this assumption to hold, we generally need to identify a large stretch of ice-free area~~This approach requires well-distributed control surfaces that cover a large enough area so that the velocity measurements are not heavily influenced by isolated hillslope movements (e.g., Brencher et al., 2021) or landslides (e.g., Shugar et al., 2021; Van Wyk de Vries et al., 2022), which are common in high-mountain environments. The central tendency (mean, median, etc.) of measured velocity components (V_x and V_y, where x and y are defined by the input image axes) over static terrain is traditionally used to calibrate the entire velocity product; see Section 3.1.2 for an example. The value of this central tendency can be regarded as the accuracy of the measured feature offset and is controlled by many factors, such as image misalignment, geolocation errors, and atmospheric disturbances (from clouds and ionosphere for optical and SAR images, respectively). In addition to the accuracy-based calibration, the ~~and their~~ residual variability (standard deviation or other similar metrics) of measured velocity components is conventionally used to assign velocity uncertainty (precision) for the entire product (Heid and Kääb, 2012; Willis et al., 2012; Burgess et al., 2013; Dehecq et al., 2015; Waechter et al., 2015; Paul et al., 2017; Millan et al., 2019). However, this variability is practically an aggregated measurement of correct and incorrect matches and other terrain-dependent errors, and it is challenging to isolate these individual contributions to total observed uncertainty. ~~A metric involving the total number and distribution of incorrect matches provides a better approach to assess the performance of a feature-tracking workflow.~~

Here, we propose a way to better characterize the noise ~~term in~~of only the correct matches for the first metric. We use non-parametric, multivariate kernel density estimation (KDE; Silverman, 1986) to differentiate correct and incorrect matches and estimate the variability of the former population. Let $V_{x,i}$ and $V_{y,i}$, $i = 1,...N$ be horizontal velocity components from the selected static area containing N measurements (i.e., N pixels). We calculate the kernel density distribution ρ_K at every possible velocity value using the following equation:

$$\rho_K(u,v) = \frac{1}{Nh} \sum_{i=1}^{N} K\left(\frac{u - V_{x,i}}{h}, \frac{v - V_{y,i}}{h}\right), \tag{1}$$

where (u,v) indicates independent variables along the x and y directions (i.e., two axes in the velocity domain), K is the selected multivariate kernel, and h is the kernel bandwidth. In other words, ρ_K resembles the histogram of the measurements or the sum of individual density distributions centered at $(V_{x,i}, V_{y,i})$. Since the choice of kernel does not affect the density estimation as much as bandwidth does, we select the Epanechnikov (parabolic) kernel to achieve computational efficiency due

to its ~~small~~finite support compared to the Gaussian kernel. We use the rule-of-thumb method (Silverman, 1986; Henderson and Parmeter, 2012) to determine the bandwidth without prior knowledge about the velocity distribution. Assuming that all the correct matches have an identical, independent, and normally distributed noise term with the same variance in u and v, the rule-of-thumb bandwidth for a multivariate Epanechnikov kernel is calculated as follows:

$$h = 2.1991\sqrt{\sigma_{V_x}\sigma_{V_y}}N^{-\frac{1}{6}}, \tag{2}$$

where σ_{V_x} and σ_{V_y} are the standard deviation of V_x and V_y, respectively. Once a kernel density distribution is found, we locate its main peak value and location on the u-v plane. This peak is assumed to be related to the distribution of the correct matches, and we can design a thresholding method based on peak value to differentiate correct and incorrect matches:

$$\rho_{K_t} = \frac{\max(\rho_K)}{e^{\frac{z^2}{2}}}, \tag{3}$$

where z is the pre-selected z score (always positive). ~~Any~~ Measurements with $\rho_K(V_x, V_y) \geq \rho_{K_t}$ are considered as correct matches, and ~~vice versa~~measurements with $\rho_K(V_x, V_y)$ lower than the same threshold value are classified as incorrect matches. The half ranges of V_x and V_y from correct matches, denoted as $\delta_u = z\sigma_u$ and $\delta_v = z\sigma_v$, are thus considered as z-sigma uncertainty. In this study, we set $z = 2$ and report two-sigma uncertainties for the convenience of comparing ~~past~~previously published results and our results. The variance of the correct matches is also defined as $\sigma_u^2 = \left(\frac{\delta_u}{z}\right)^2$ and $\sigma_v^2 = \left(\frac{\delta_v}{z}\right)^2$.

To summarize, while statistics computed over static terrain have previously been used to assess the uncertainty of glacier velocity maps, this study attempts to separate correct and incorrect feature matches over static terrain, and derive uncertainty only from the correct matches. The calculated uncertainty of correct matches can be compared with the theoretical uncertainty (Sciacchitano, 2019). Ideally, the former should approach the latter for optimized measurement precision. In addition, the number of incorrect matches over static terrain and their corresponding velocity distribution can serve as an auxiliary indicator of the accuracy of the velocity map, along with the correct-match uncertainty.

2.2   Metric 2: along-flow strain rates

~~Our~~For computational simplicity, our previous metric overlooks the covariance of the correct matches ~~for computational simplicity~~. However, glacier motion is spatially coherent, and the covariance of neighboring correct matches controls the quality of the measured flow pattern. Hence, the second metric aims to estimate the co-variability of pixels on a glacier using the physics of glacier flow (Cuffey and Paterson, 2010). We start by analyzing the horizontal (2-D) strain rate tensor $\dot{\epsilon}_{x'x'}$, $\dot{\epsilon}_{y'y'}$, and $\dot{\epsilon}_{x'y'}$, where the prime notations of x' and y' denote along-flow and across-flow directions, respectively. To obtain this tensor, we first calculate the strain rates along the image axes x and y:

$$\dot{\epsilon}_{xx} = \frac{\partial V_x}{\partial x}$$
$$\dot{\epsilon}_{yy} = \frac{\partial V_y}{\partial y} \tag{4}$$
$$\dot{\epsilon}_{xy} = \frac{1}{2}\left(\frac{\partial V_x}{\partial y} + \frac{\partial V_y}{\partial x}\right)$$

In GLAFT, these partial derivatives are computed using 3-by-3 Sobel operators. Next, we compute $\arctan2(V_x/V_y)$ and smooth the results with a 2D median filter with a large window size of 10–35 pixels (depending on the pixel spacing) for the bulk flow direction angle θ (counterclockwise from the x-axis). The strain rate tensor is then rotated by θ and projected into the along-flow direction as follows:

$$\dot{\epsilon}_{x'x'} = \dot{\epsilon}_{xx}\cos^2\theta + \dot{\epsilon}_{yy}\sin^2\theta + \dot{\epsilon}_{xy}\sin 2\theta$$
$$\dot{\epsilon}_{y'y'} = \dot{\epsilon}_{xx}\sin^2\theta + \dot{\epsilon}_{yy}\cos^2\theta - \dot{\epsilon}_{xy}\sin 2\theta \tag{5}$$
$$\dot{\epsilon}_{x'y'} = \frac{1}{2}(\dot{\epsilon}_{yy} - \dot{\epsilon}_{xx})\sin 2\theta + \dot{\epsilon}_{xy}\cos 2\theta$$

By replacing V_x and V_y with $\dot{\epsilon}_{x'x'}$ and $\dot{\epsilon}_{x'y'}$ in Equation 1, we can calculate the KDE in the strain rate domain and characterize the distribution. We follow the same steps in Equations 2–3 and find the variance of the strain rate distribution under a pre-selected z value. To be consistent with the first metric, in this study we report the z-σ uncertainty for $\dot{\epsilon}_{x'x'}$ and $\dot{\epsilon}_{x'y'}$ as $\delta_{x'x'}$ and $\delta_{x'y'}$, respectively.

Unlike the case of the previous metric, which indicates the variability from the zero ground truth, the strain rates along a flowing glacier are not zero, but we can still infer a reasonable range based on fundamental physical relationships. Consider a rectangular region on a glacier with one side running across the channel half-width Y and the other side along the flow direction (length X). The average driving stress ($\bar{\tau}_d$) over the rectangular area is balanced with the basal drag ($\bar{\tau}_b$), side drag, and longitudinal stress gradient (see Equation 8.60 of Cuffey and Paterson, 2010, for details):

$$\bar{\tau}_d = \bar{\tau}_b + \frac{1}{Y}\Delta(H\bar{\tau}_{x'y'}) + \frac{1}{X}\Delta[H(2\bar{\tau}_{x'x'} + \bar{\tau}_{y'y'})], \tag{6}$$

where H is average ice thickness. $\bar{\tau}_{x'y'}$, $\bar{\tau}_{x'x'}$, and $\bar{\tau}_{y'y'}$ represent average shear stress and normal stresses, respectively. Suppose half of the driving stress is balanced by basal drag, and the other half is balanced by side drag, and the longitudinal stress gradient is negligible (cf. Table 8.3 of Cuffey and Paterson, 2010), Equation 6 becomes

$$\bar{\tau}_b = \frac{1}{Y}\bar{\tau}_{x'y'}\Delta H. \tag{7}$$

For the right-hand side of Equation 7, we let $\Delta H \approx H$, indicating the maximum possible ice thickness change within the rectangular region. Moreover, we can express the average side drag as a function of the average strain rate, assuming glacier

ice can be modeled as a viscous non-Newtonian fluid with the following creep relation (Equation 3.23 of Cuffey and Paterson, 2010):

$$\tau_{jk} = 2\eta\dot{\epsilon}_{jk},\tag{8}$$

where η is ice viscosity, and the subscripted j and k denote any two of the three dimensions. Thus, Equation 7 becomes

170

$$\bar{\tau}_b = \frac{1}{Y}2\eta\bar{\dot{\epsilon}}_{x'y'}H,\tag{9}$$

where $\bar{\dot{\epsilon}}_{x'y'}$ is the average shear strain rate.

The creep relation (Equation 8) can also be expressed inversely, known as Glen's flow law:

$$\dot{\epsilon}_{jk} = A\tau_{jk}^n,\tag{10}$$

where n and A are two empirical parameters. Combining Equations 8 and 10 leads to the expression of viscosity in terms of

175 the flow-law parameters:

$$\eta = \frac{1}{2A\tau_{jk}^{n-1}}.\tag{11}$$

The along-flow ice speed at the surface ($u_{x'}$) can be calculated by integrating Glen's flow law (Equation 10) along the vertical direction of the ice flow plus the basal slip speed (u_b), assuming a linearly increasing shear stress with depth (see Equations 8.32 to 8.35 of Cuffey and Paterson, 2010, for details):

180

$$u_{x'} = u_b + \frac{2A}{n+1}\tau_b^n H.\tag{12}$$

Combining Equations 11 and 12 with τ_{jk} set to τ_b leads to the expression of average basal drag as a function of average surface along-flow speed $\bar{u}_{x'}$ and average basal slip speed $\bar{u}_b$:

$$\bar{\tau}_b \approx (\bar{u}_{x'} - \bar{u}_b)\eta\frac{n+1}{H}.\tag{13}$$

Finally, combining Equations 9 and 13 leads to the following equation:

185

$$\frac{\bar{\dot{\epsilon}}_{x'y'}}{\bar{u}_{x'} - \bar{u}_b} = \frac{(n+1)Y}{2H^2},\tag{14}$$

which can be further reduced to $2Y/H^2$ if assuming $n = 3$.

Equation 14 provides a range of plausible $\dot{\epsilon}_{x'y'}$ values based on glacier speed, channel width, and average ice thickness. Ideally, observed $\delta_{x'y'}$ should be as close to $\bar{\dot{\epsilon}}_{x'y'}$ as possible. If the former is much larger, the glacier velocity likely contains errors, as the observed spatial variability is not physically achievable. On the other hand, if $\bar{\dot{\epsilon}}_{x'y'}$ is much larger than $\delta_{x'y'}$, it is likely that the flow pattern is smoothed too much and has lost real dynamic signals.

3 Tests at Kaskawulsh Glacier

Kaskawulsh Glacier, Yukon, Canada (60°48′N, 138°36′W; Figure 1) is an ideal location for demonstrating how these metrics relate to the performance of feature-tracking workflows because it has a nearly continuous GNSS record since ~~2009~~2007, is a wide and long glacier with relatively consistent velocities, and does not surge (Clarke et al., 1986). Kaskawulsh Glacier has an area of 1054 km^2, stretches ∼90 km from the terminus to the farthest ice divide (RGI Consortium, 2017), and has velocities along the main trunk of the glacier ranging from 70 m yr^{-1} near the terminus to 180 m yr^{-1} near the confluence of the two main tributaries (Waechter et al., 2015; Gardner et al., 2019). ~~Due to~~ The recent terminus retreat of Kaskawulsh Glacier ~~regional water patterns shifted~~changed the local hydrology, resulting in a drop in water level at Łù'àn Män (Kluane Lake), which has impacted indigenous people in the area (Shugar et al., 2017).

Kaskawulsh Glacier has been a research site for decades with a history of velocity observations dating back to the 1960s. The Icefield Ranges Research Project set up a network of markers to track glacier motion during the 1960s, which concluded there were limited short-term variations in ice velocity (Holdsworth, 1969; Clarke, 2014). More recent work has focused on regional velocity patterns (Burgess et al., 2013; Abe and Furuya, 2015; Waechter et al., 2015; Van Wychen et al., 2018; Altena et al., 2019) and found a multi-year acceleration near Kaskawulsh Glacier's terminus as a terminal lake grew from 2000–2015, followed by a slowdown over the following five years after it drained in 2016 (Main et al., 2022).

3.1 Methods

3.1.1 Deriving glacier velocities

We selected four optical satellite image pairs (Figure 1, Table 1), each of which has a different time separation and surface conditions. We downloaded ~~them~~the Level-2 orthorectified images from the USGS EarthExplorer (https://earthexplorer.usgs.gov/) and clipped them to the extent of Kaskawulsh Glacier for processing efficiency. We used four different packages to derive glacier velocity maps, each of which has a distinct method for processing velocity fields, briefly described as follows:

– **autoRIFT** (autonomous Repeat Image Feature Tracking; Lei et al., 2021): an open-source feature tracking toolbox developed at NASA JPL, written in Python and C++, autoRIFT performs normalized cross-correlation (NCC) in the spatial domain using either a fixed or adaptive size of matching template. The software can perform pre-processing to enhance image contrast and improve feature details prior to feature tracking. For post-tracking processes, autoRIFT uses a novel Normalized Displacement Coherence (NDC) filter to remove pixels whose displacement is inconsistent with
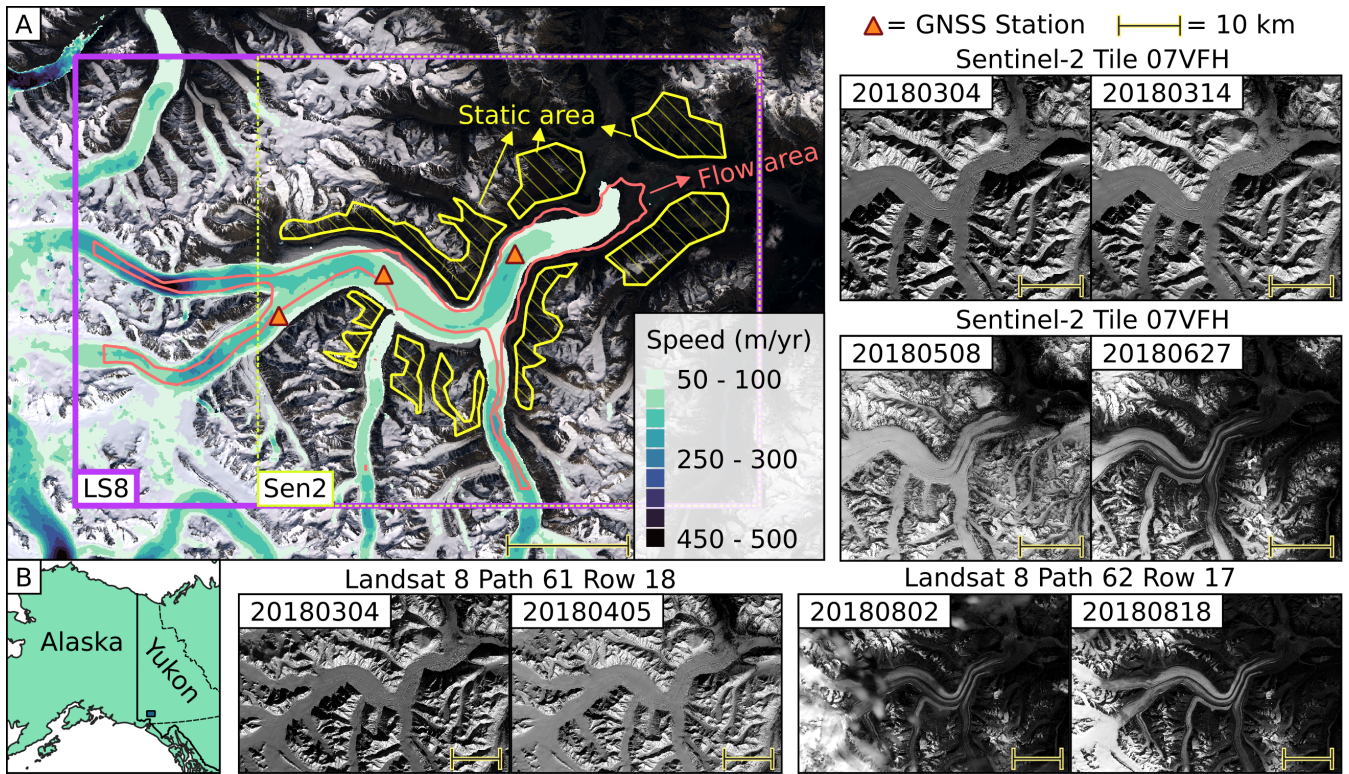
Figure 1. Kaskawulsh Glacier and satellite images used to derive velocity testing maps. **(a)** Time-averaged glacier velocity (Millan et al., 2022) plotted on a Landsat 8 natural color composite from June 9, 2016. Areas for deriving the proposed metrics are labeled with two types of polygons: static areas in hashed yellow, and flow areas in red. Triangles indicate GNSS station positions in 2018. Rectangles show extents of the clipped Landsat 8 (purple) and Sentinel-2 (yellow) images used in this study. **(b)** Context map for panel a. Other panels show the clipped images with labels specifying their respective tile numbers and acquisition dates.

Table 1. Optical images used to derive glacier velocities in this study.

Satellite	Band	Image 1 date	Image 2 date	Duration (days)	Pixel spacing (m)
Landsat 8	8 (500-680 nm)	2018-03-04	2018-04-05	32	15
Landsat 8	8 (500-680 nm)	2018-08-02	2018-08-18	16	15
Sentinel-2	4 (665 nm)	2018-03-04	2018-03-14	10	10
Sentinel-2	4 (665 nm)	2018-05-08	2018-06-27	50	10

neighboring pixels. OpenCV's Laplacian pyramid method (abbreviated as pyrUP in Table S1; Bradski, 2000) is used to upsample the results for subpixel precision. A specially curated parameter set is used with autoRIFT to generate ITS_LIVE, the largest open data set for glacier velocity (Gardner et al., 2019).

- **vmap** (Shean and Bhushan, 2023): an open-source feature tracking software package written in Python ~~it uses~~that wraps the C++ based NASA Ames Stereo Pipeline (ASP) pyramidal correlator ~~scheme~~ (Beyer et al., 2018) to perform NCC in the spatial domain. Images can be pre-processed using ~~ASP's built-in~~a Gaussian or Laplacian of Gaussian operator, and ~~correlation~~ results are filtered to remove ~~erroneous~~spurious measurements. Vmap supports three methods for calculating displacements with sub-pixel precision, defined as parabolic (Argyriou and Vlachos, 2005), affine, and affine adaptive (Nefian et al., 2009; Baker and Matthews, 2004; Broxton et al., 2009) ~~in this study~~. We refer readers to ~~Section 93 in Stereo-Pipeline~~the official ASP documentation (https://stereopipeline.readthedocs.io/en/latest/index.html) for additional details on the correlation and sub-pixel refinement ~~procedures~~options.

- **CARST** (Cryosphere And Remote Sensing Toolkit; Zheng et al., 2021): an open-source glacier remote sensing package written in Python, its feature tracking functionality is a Python wrapper of ampcor, a Fortran module developed by NASA JPL as part of the SAR processing package ROI_PAC (Rosen et al., 2004) and its successor ISCE (Rosen et al., 2012). Ampcor uses NCC in the spatial domain to perform the tracking and deploys a simple oversampling method for sub-pixel precision.

- **GIV** (Glacier Image Velocimetry; Van Wyk de Vries and Wickert, 2021): an open-source package designed for calculating glacier velocity fields using MATLAB or a standalone app. GIV is optimized for the automated processing of entire time series of satellite imagery, but can also be used to process single image pairs. Unlike the other packages mentioned here, GIV matches ~~images~~features in the frequency domain. Additionally, GIV includes an orientation filter for image pre-processing named "near anisotropic orientation filter" (NAOF), which is used as a pre-processing option for the source images (Table S1). GIV also uses the "multi-pass" method that matches ~~images~~features multiple times using decreasing template sizes. In our tests, this multi-pass method uses template sizes of 24 to 6 pixels for Sentinel-2 images and 16 to 4 pixels for Landsat 8 images, which is smaller than the other fixed template sizes tested in this study (32 or 64 pixels).

We selected a total of 172 distinct combinations of parameters for software tool, pre-filter, matching window size (chip size), skip size (velocity grid spacing), and sub-pixel mode (Table S1; see supplemental Jupyter Book pages in Data Availability section). ~~Not all available settings can be applied (e.g., Vmap only accepts the built-in Gaussian or Laplacian of Gaussian pre-filters and does not accept externally pre-filtered images, such as NAOF). In addition,~~ We do not have an equal number of tests for each software tool as ~~the goal is~~this study aims to ~~validate the usefulness of the~~evaluate our metrics, not to compare ~~and determine which tool is the best.~~the performance of the different tools. To calculate our metrics, we used resulting velocity map products ~~from the feature tracking tools~~ without additional corrections such as bias or noise removal. We manually selected static and ice flow regions, as shown in Figure 1. ~~We set the z value to 2 in all of our workflows.~~ See Data Availability for all the corresponding code and scripts.

3.1.2 GNSS data processing

Three GNSS stations have been operating on Kaskawulsh Glacier since 2007 (Figure 1), providing a nearly continuous record of glacier velocity in three dimensions. These stations consist of a Trimble NetR9 receiver with a Zephyr Geodetic Antenna (Trimble R7 receiver prior to 2016), large rechargeable sealed lead acid batteries, a solar panel, and solar regulator.

During the summer (approximately May to September) these stations operate 24 hours per day, recording observables that can be used to determine the antenna position every 15 seconds. During the winter (approximately September to May) the stations are set to conserve power and typically only record data every 15 seconds for two to three hours per day starting at noon local time, providing daily observations of glacier motion.

The GNSS data were recorded in proprietary Trimble format and converted to the open RINEX format during post-processing. We used the kinematic precise point positioning (PPP) processing service offered by Natural Resources Canada (https://webapp.geod.nrcan.gc.ca/geod/tools-outils/ppp.php?locale=en) to obtain refined GNSS positions for this study. We used a custom python script to derive horizontal velocity from the GNSS positions that most closely match the time of satellite image acquisitions. Three-dimensional position uncertainties are approximately 2 cm over a one-hour observation window (Thomson and Copland, 2017). Typical horizontal velocities at Kaskawulsh Glacier at these stations are ~0.30 to 0.50 m per day.

To compare the 172 velocity maps with GNSS data, the former have to be calibrated to reduce systematic biases due to image misalignment. This bias correction is achieved by subtracting the KDE peak location of the static terrain velocities (i.e., u and v that has value of $\max(\rho_K)$; see Equation 3.) To sample measurements from a velocity map at the location of the GNSS stations, we used the geoutils package (version 0.0.9, https://pypi.org/project/geoutils/) to extract the nearest-neighbor pixel values for the GNSS station locations at the ~~beginning of the acquisition duration.~~acquisition time of the earlier image in the pair.

3.1.3 Deriving metrics from the ITS_LIVE velocity maps

We downloaded 35 scene-pair velocity maps from the ITS_LIVE data search portal (see Data Availability). These velocity maps were derived using Landsat 8 or Sentinel-2 source images from the same orbital tracks specified in Figure 1 and Table 1, acquired between March 4 and October 5, 2018. The complete list of the velocity maps is available in Table S3. We use the value of the `Vx_err` flag that comes with each velocity map as the one-sigma error of the V_x velocity component ~~(i.e., half of the y value for each point in Figure 7)~~. We follow the same methods defined in this study (Equations 1–14) and the GLAFT tool to compute δ_u and $\delta_{x'y'}$ using the same static area and flow outlines defined in Figure 1. ~~The data used to plot Figure 7 are available in Table S4.~~

3.1.4 Synthetic offset test

We created two synthetic sub-pixel offset fields with the same dimensions as the Landsat 8 satellite image acquired on March 4, 2018 (Table 1). Each offset field varies along a single image axis (~~E/W or N/S; Figure 6a~~x or y). We applied these ~~E/W and N/S~~x and y offset fields to the input satellite image and generate a synthetic satellite image with offset features. Next, we performed feature tracking between the original image and the synthetically shifted image using the vmap software. For feature tracking parameters, we used a matching window size of 35 pixels and parabolic subpixel refinement. ~~The resulting offset maps in the E/W and N/S directions are shown in Figure 6b.~~

3.2 Results

285 Our 172 glacier velocity maps (six in Figure 2 and the rest in Figures S1–S8) are similar to the time-averaged speed from Millan et al. (2022) shown in Figure 1: the average flow speed is around 0.3 m/day (100 m/yr), with ~~slight regional~~small local variations. While it is common to clip velocity maps to glacier outlines in publications and data sets, we show the full velocity map for each test so that readers can see the distribution of invalid and incorrect matches over adjacent terrain. For the examples in Figure 2, the bad matches (empty and unrealistic values in each upper panel) roughly align with the changing illumination

290 and corresponding shadow positions during the image acquisition period (March to April 2018). These six maps show δ_u and δ_v ranging from 0.06 to 0.64 m/day. For every velocity map, ~~has similar δ_u and δ_v values, probably~~δ_u and δ_v are close in value, likely because a square matching template was used to track features. Therefore, we use δ_u as Metric 1 to assess the velocity map quality in the rest of the study. Large δ_u values generally indicate a noisy velocity map, and small δ_u corresponds to a smoother velocity field (Figure 2a-c). Besides the magnitude of Metric 1, velocity maps generated by different software packages show

295 various clustering characteristics over static terrain ~~velocity distribution~~. For example, maps derived using vmap and autoRIFT often have elongated, off-zero clusters ~~with unclear cause~~ (Figure 2c–d), while maps from CARST and GIV ~~processed velocity maps have different levels of~~contain artifacts due to the pixel locking effect (Figure 2e–f), a biased tendency that measurements, including incorrect matches, favor integer pixel offsets (Shimizu and Okutomi, 2001; Stein et al., 2006). Other results derived from the rest of the tests are available in Figures S9–S16 and Table S2.

300 Unlike the static terrain velocities, the along-flow strain rate does not show characteristic spatial variability across most tests; these values tend to ~~plot as~~form a single cluster centered on zero (Figure 3 bottom panels; also Figures S17–S24). The variability of the normal and shear strain rates is similar, as indicated by similar $\delta_{x'x'}$ and $\delta_{x'y'}$ values. This suggests that random noise, not glacier physics, controls such variability. The magnitude of $\delta_{x'y'}$ (Metric 2) does not show an obvious correlation to the velocity map (Figure 3 upper panels), but a closer inspection by plotting the overall strain rate magnitude ($\sqrt{\dot\epsilon_{x'x'}^2 + \dot\epsilon_{x'y'}^2}$)

305 shows that $\delta_{x'y'}$ relates to the smoothness of the strain rate map (Figure 3 middle panels). Metric 2 is insensitive to correlated error over long spatial scales (Figure 3c), but is sensitive to high-frequency spatial variation with ~~even a~~ small amplitude (Figure 3a). ~~Our 172 tests show~~The $\delta_{x'y'}$ and $\delta_{x'x'}$ values range from 0.001 to 0.12 day^{-1} across the 172 velocity maps (Figures S17–S28 and Table S2).

3.2.1 ~~Intercomparison~~Relationship between the metrics, tracking parameters, and velocity map quality

310 As expected, the values of Metric 1 (δ_u) and 2 ($\delta_{x'y'}$) vary across the 172 tests depending on multiple parameter selections. For example, when the satellite images are high-pass filtered before computing the cross-correlation surface, the resulting velocity maps often display improved quality as represented by a low δ_u value (Figure 4a). This observation aligns with several past studies (Dehecq et al., 2015; Fahnestock et al., 2016; Van Wyk de Vries and Wickert, 2021). The δ_u values also decrease with increasing matching template size, a classic trade-off between spatial smoothing and noise (Ahn and Howat, 2011, Figure 4b).

315 We can also see ~~trends related to~~systematic variation in $\delta_{x'y'}$: it generally decreases as output velocity map resolution (pixel size) increases, with a minimum of ~0.004 day^{-1} (Figure 4c). Substituting representative values for Kaskawulsh Glacier into
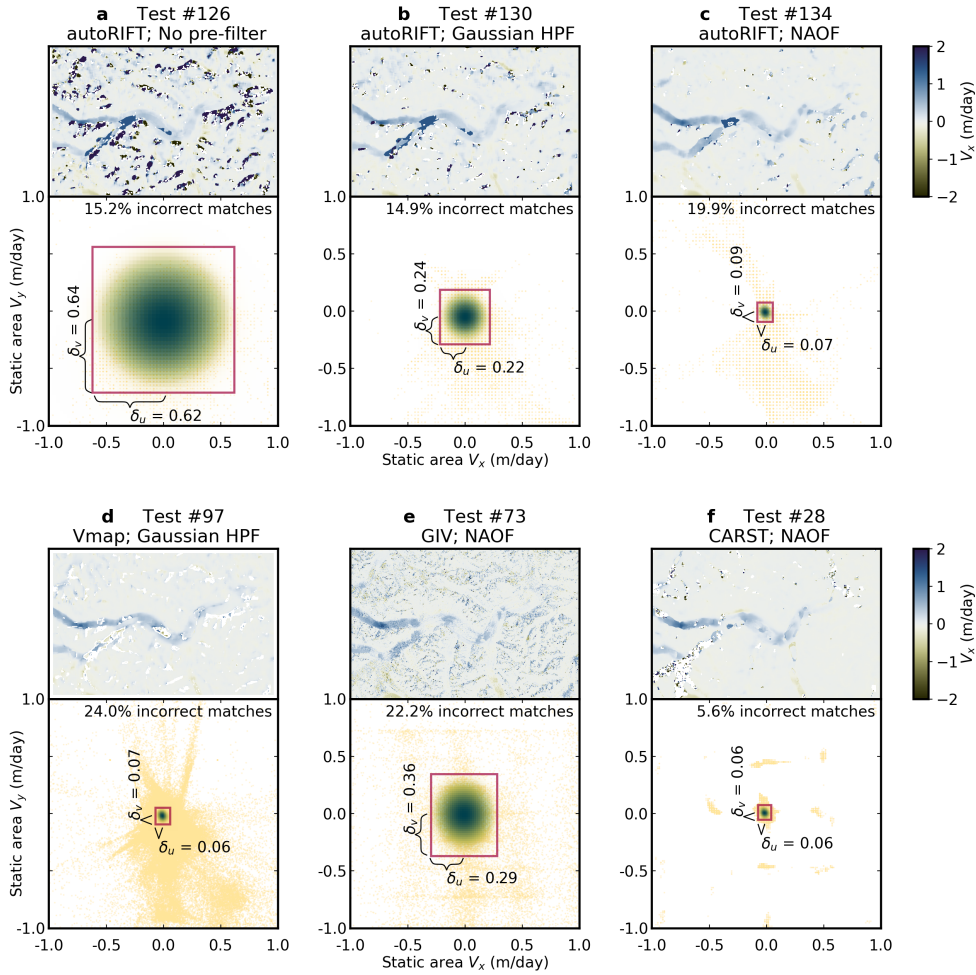
Figure 2. Feature tracking results and static area velocities for the Landsat 8 pair 20180304-20180405 using six different parameter sets. Each subpanel includes a map of the E-W velocity component (V_x) in the top and the distribution of static-terrain velocities (yellow dots) with their kernel density estimate (KDE) in the bottom. The red box indicates the boundary where KDE drops to $1/e^{\frac{z^2}{2}}$ of the peak KDE reading. Measurements falling outside the red box are labeled as incorrect matches, with the ratio to the total number of static area measurements shown on the plot. The half-width and height of the box are assigned as δ_u and δ_v, respectively, with their value shown in the plot. **(a-c)** Sample tests derived using autoRIFT with different pre-filters. **(d-f)** Sample tests derived using vmap, GIV, and CARST, respectively. See Table S1 for the full parameters corresponding to each test.

Equation 14 (H = 700 m (Foy et al., 2011), Y = 3500 m, $\bar{u}_{x'}$ = 0.3 m/day, and $\bar{u}_b$ = 0 m/day), we obtain a recommended value of 0.004 day^{-1} for $\delta_{x'y'}$. Note that we assume no basal slip in this calculation, which may not be physically realistic for Kaskawulsh Glacier and likely yields an overestimated $\delta_{x'y'}$ recommendation. Nevertheless, these two independent computations suggest 320 that, in our case, velocity maps with an output ~~resolution~~grid cell size equal to or larger than 8x the input pixel size should have
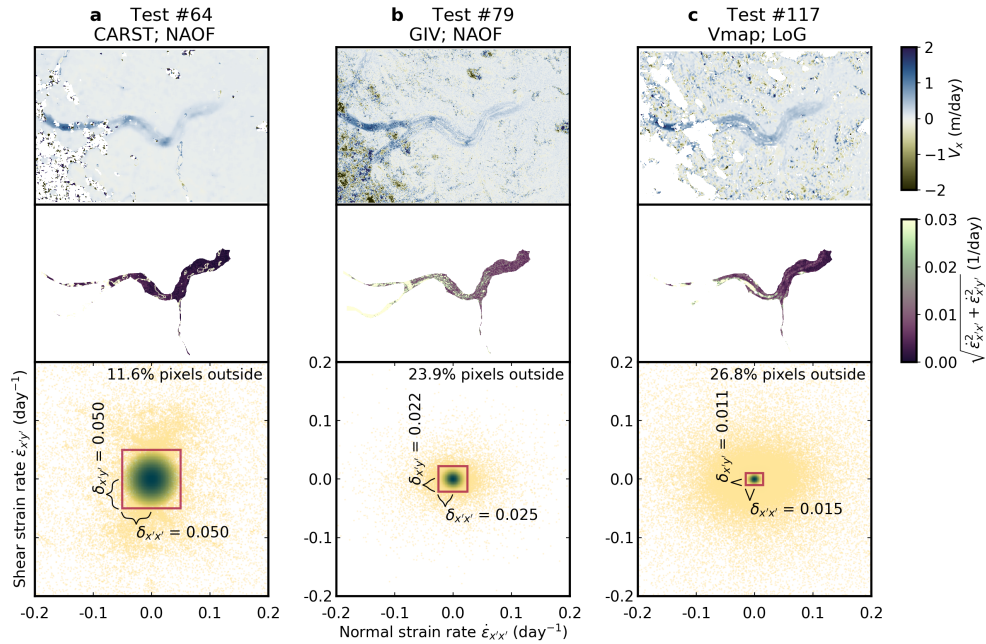
Figure 3. Feature tracking results and flow strain rate of the Landsat 8 pair 20180802-20180818 using three different parameter sets. Each subpanel includes a map of the E-W velocity component (V_x) at the top, map of strain rate magnitude in the middle, and scatterplot showing the strain rate distribution (yellow dots) with their kernel density estimate (KDE) at the bottom. The red box indicates the boundary where KDE drops to $1/e^{\frac{z^2}{2}}$ of the peak KDE reading. The half-width and height of the box are assigned as $\delta_{x'x'}$ and $\delta_{x'y'}$, respectively, with their value shown in the plot. See Table S1 for the full parameters corresponding to each test number.

better quality because the observed strain rate is constrained by glacier physics. On the other hand, the observed strain rate in velocity maps with a finer output ~~resolution~~grid cell size of 1x or 4x the input pixel size should be dominated by large feature matching uncertainty.

325   A combined analysis of the two metrics offers a more powerful quality indicator for glacier velocity maps. Maps with higher δ_u and $\delta_{x'y'}$ values tend to have fewer correct matches (Figure 5a). Again, the recommended value of $\delta_{x'y'}$ based on glacier physics (0.004 day⁻¹ for Kaskawulsh, ~~based on~~ Equation 14) seems to play an important role. All the maps with $\delta_{x'y'}$ less than this threshold value have at least 50% correct matches (Figure 5a). These results strongly support the ~~argument~~hypothesis that the uncertainty of correct matches ~~links to~~depends on the prominence of the cross-correlation peak. ~~which also affects how likely a tracking algorithm locates a false peak and yields an incorrect match.~~
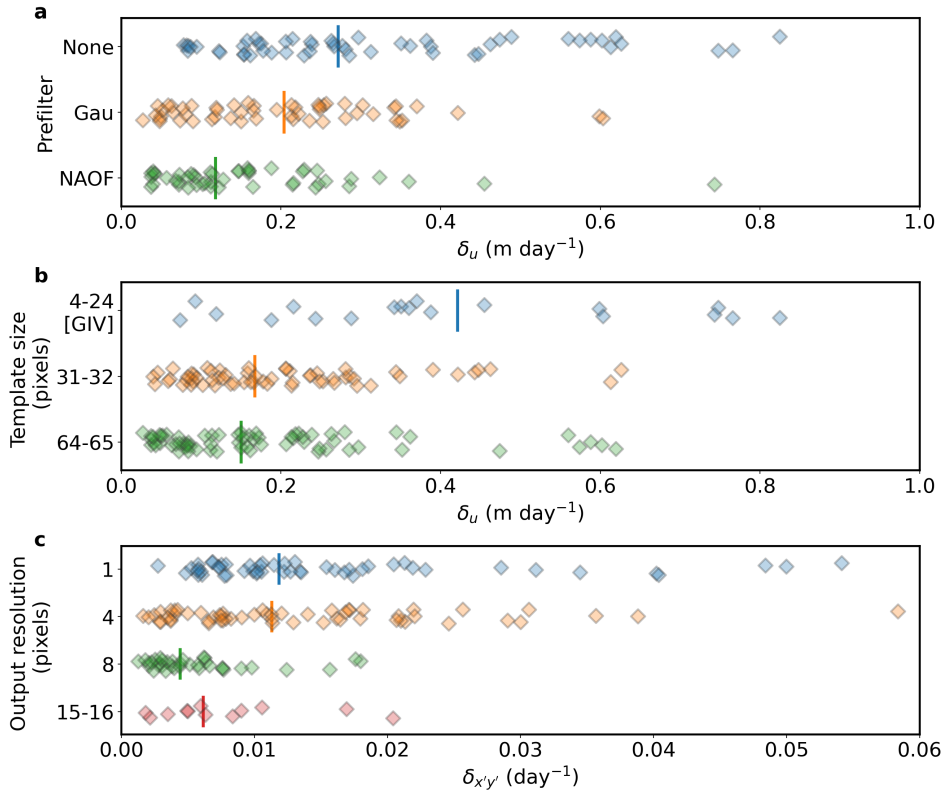
Figure 4. Relationship between selected velocity map generation parameters and our velocity map quality metrics. Each panel is a 1-D scatter plot showing different parameter choices used during the feature tracking process versus the derived metric. Each point represents a different test result. Vertical bar indicates the median value of each subgroup. **(a)** Prefilter vs. δ_u (Metric 1). **(b)** Matching template size vs. δ_u (Metric 1). See the description of GIV in Methods for its different approach regarding the template size. **(c)** Output resolution vs. $\delta_{x'y'}$ (Metric 2).

330 ### 3.2.2 ~~Additional test using~~ Comparison with in situ measurements and synthetic offset test

We find that a considerable number of velocity maps (73 out of 172) have speed deviation (in the V_x component) from the GNSS ground truth data larger than their δ_u, the two-sigma ~~correct match~~ uncertainty over static terrain (Figure 5b). Maps with higher $\delta_{x'y'}$ are more likely to show this deviation. In fact, the deviation cannot simply be explained by the inclusion of incorrect matches, which should only be around 6-24% according to Figure 2 and Table S2. We argue that this deviation is

335 related to the fact that correct matches on the glacier surface have a different noise distribution than those on the static terrain, potentially related to differences in the ~~topographic roughness and surface reflectance~~ local variance of surface topography (roughness) and reflectance (texture) between static and ice surfaces (Paul et al., 2017). ~~To test this idea, we performed an additional feature tracking test using an image pair derived from a single image with an arbitrary, synthetic velocity field.~~ The synthetic offset test results (Section 3.1.4) ~~show a noisier velocity pattern~~ support this hypothesis, with more spurious matches and noise observed on the glacier surface compared
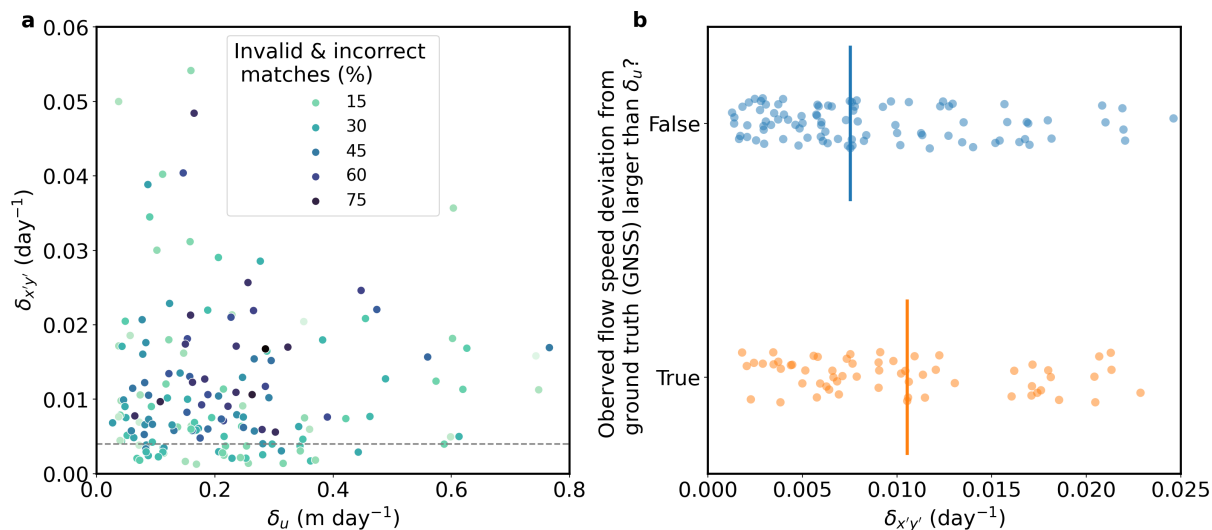
Figure 5. Relationship between our metrics and velocity map quality. **(a)** Values for $\delta_{x'y'}$ (Metric 2) versus δ_u (Metric 1) for all 172 tests, with point color showing the percentage of invalid (NoData) and incorrect matches in the corresponding output velocity map. Gray dashed line indicates where $\delta_{x'y'} = 0.004$ day^{-1} (see text). **(b)** 1-D scatter plot showing observed flow speed deviation from the ground truth (GNSS) versus $\delta_{x'y'}$ (Metric 2). The deviation is grouped by whether it is larger than the inferred uncertainty of correct matches (δ_u; Metric 1). Ver-tical bars represent the median values of the corresponding groups.

to the static terrain (Figure 6). ~~strongly suggesting~~This finding suggests that correct matches on the glacier surface inherently have larger uncertainty.

4   Discussion

The correct-match uncertainty (δ_u and δ_v) is theoretically smaller than the bulk variability (e.g., standard derivation) computed from mixed correct and incorrect matches, ~~which can also be seen in a real data set.~~which is true for the data evaluated in this study. For example, each ITS_LIVE scene-pair glacier velocity map for Kaskawulsh Glacier during 2018 is distributed with an internally calculated standard deviation of static terrain velocities as uncertainty. These two-sigma errors ~~of all maps are always~~are larger than the corresponding δ_u or δ_v values (Figure 7 for V_x; see Section 3.1.3 for details). Since the uncertainty of incorrect matches is large and unpredictable, we argue that only correct-match uncertainty should be considered ~~as the~~when evaluating velocity map quality.

Although δ_u and δ_v are good quality indicators, they are not good estimators for the uncertainty of the ice velocity. This is because (1) ice velocities also contain incorrect matches, and (2) ice velocities have a different noise distribution than static terrain velocities (Figure 6). Attempts using static area velocity statistics to assign ice velocity uncertainty are likely to show many outliers when compared with ground truth data (e.g., Figure 5b in this study and Figure 6 of Redpath et al., 2013). Nevertheless, minimizing δ_u and δ_v is still important because low correct match uncertainty relates to low bulk variability
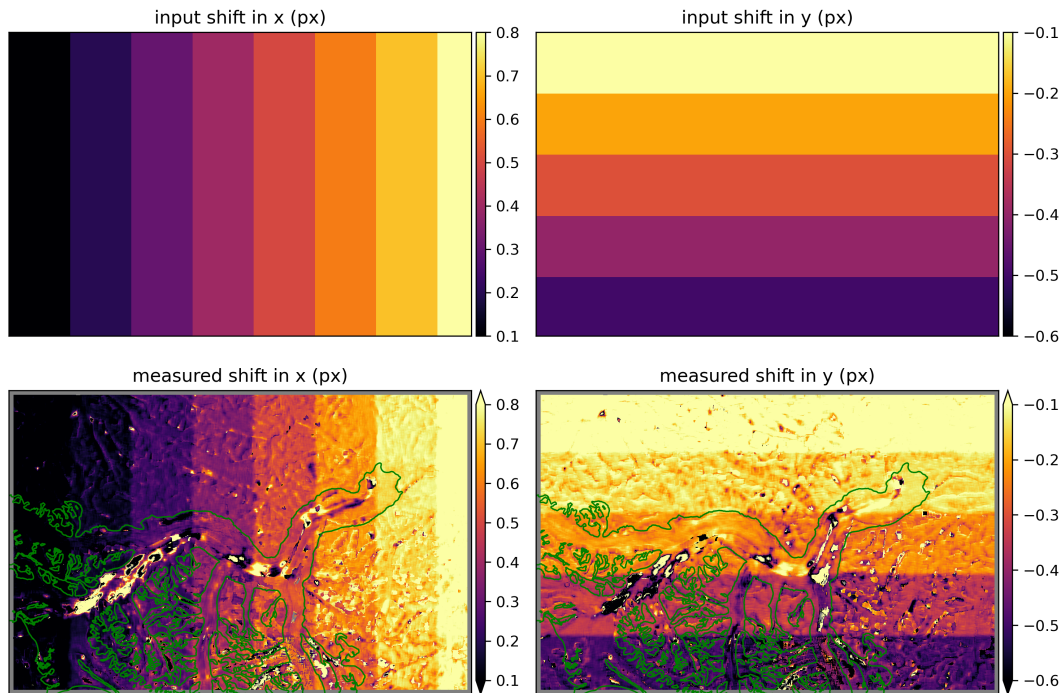
Figure 6. Feature tracking tests using synthetic offset fields (Section 3.1.4). **(a)** The x and y components of the synthetic offset field applied to a single Landsat 8 image acquired on 20180304 (Table 1). **(b)** Feature tracking results (vmap, kernel size = 35px, parabolic subpixel refinement) show a larger deviation on ~~the glacier~~Kaskawulsh Glacier surface (green polygons) than the static areas. ~~(see glacier outline in Figure 1).~~

355   (Figure 6) and reduces the chance of an invalid or incorrect match (Figure 5a). It is also worth examining the pattern of incorrect matches discovered during the same workflow (Figure 2) for efficient mitigation.

The variability of flow strain rate provides a second way to assess the quality of glacier velocity maps. Larger $\delta_{x'y'}$ correlates to more bad matches (Figure 5a), leading to lower overall accuracy (Figure 5b) and a higher bulk uncertainty (Figure 7). It is thus essential to ensure that the velocity map has certain spatial coherence to minimize $\delta_{x'y'}$ until it decreases to a suggested

360   value based on ice flow physics (Equation 14). Without spatial smoothing, it may not be possible for $\delta_{x'y'}$ to go below that threshold value (Figure 4c). Velocity maps with $\delta_{x'y'}$ near the threshold value theoretically have a coherent, less error-prone, and physically meaningful strain rate field, which is critical for glacier modeling.

4.1   Recommended strategy to evaluate velocity map quality

The metrics presented in this paper can be used to assess the quality of glacier velocity maps (Table 2). We suggest that the

365   correct-match uncertainty of static terrain velocity, δ_u (and δ_v if the map is derived using a ~~rectangular~~non-square matching
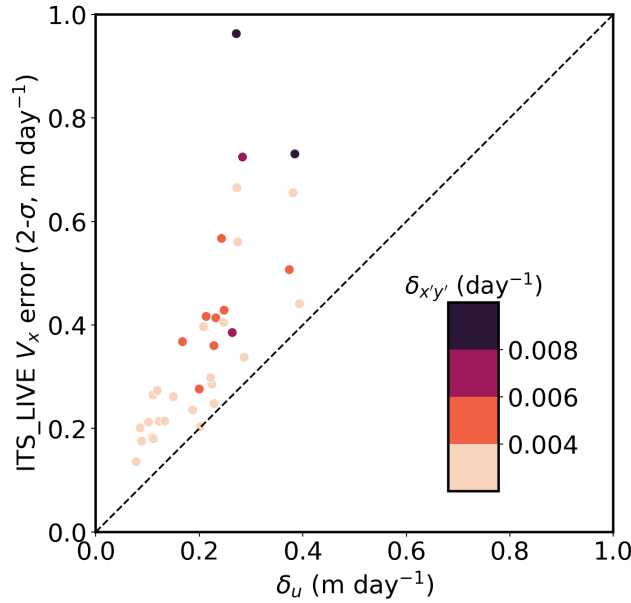
Figure 7. Comparison of reported ITS_LIVE V_x error (2× the `Vx_err` value from original metadata) with our derived correct-match δ_u uncertainty (metric 1) for 35 velocity maps. Each point represents a scene pair listed in Table S3, with color showing the corresponding uncertainty of the glacier shear strain rate (Metric 2). The dashed line indicates the 1:1 ratio of the two axes. Data used to prepare this figure are available in Table S4.

template, which is common for SAR feature tracking), should be as low as possible until the value reflects the inherent match uncertainty only. If the inherent match uncertainty (2-sigma) is 0.2 pixels (Sciacchitano, 2019), the desired range of δ_u is

$$\delta_u \leq 0.2 \times \frac{\text{pixel size of source images}}{\text{duration of source image pair}}. \tag{15}$$

The recommended value for the variability of along-flow shear strain rate, $\delta_{x'y'}$, depends on the flow-law parameter n and

370 basal sliding velocity $\bar{u}_b$ (Equation 14), which can be challenging to measure. However, based on the test results presented in this study, proposing an overestimated value by setting zero basal slip may be acceptable because it is more conservative on whether the observed strain rate field links to the actual ice flow dynamics. With the general assumption of $n = 3$, we suggest the following guideline for setting a $\delta_{x'y'}$ threshold, which relates to the average surface along-flow speed $\bar{u}_{x'}$, channel half width Y, and average ice thickness H:

375 $$\delta_{x'y'} \approx \bar{u}_{x'} \frac{2Y}{H^2}. \tag{16}$$

We can apply these metrics and guidelines in various use cases, and here are some practical examples. Users who run feature-tracking workflows can compute these metrics for their output velocity maps. If a velocity map has either metric deviates from

Table 2. Summary of using static terrain velocities and along-flow strain rates to assess glacier velocity maps.

Name	How to calculate using GLAFT	Recommended value
Correct-match uncertainty of static terrain velocity (δ_u or δ_v)	glaft.Velocity.static_terrain_analysis() (Equations 1–3)	based on the inherent match uncertainty (Equation 15)
Variability of along-flow shear strain rate ($\delta_{x'y'}$)	glaft.Velocity.longitudinal_shear_analysis() (Equations 4–5)	$\bar{u}_{x'} \frac{2Y}{H^2}$ (Equation 16)

the ~~suggested value~~recommended range, they can try a different parameter combination, including prefilters, tracking parameters, subsampling, masking, and other post ~~processes, and optimize the map by approximating the metrics to~~processing steps until the metrics fall within the recommended values. In addition to these metrics, the users can analyze the number and spatial distribution of incorrect matches over the static terrain to identify directions of improvement; see Figure 2 and discussion in Section 3.2 for an example. ~~For novel tracking algorithms,~~ These metrics will also serve as a basis for comparing novel feature tracking algorithms (e.g., Altena and Kääb, 2020) with traditional algorithms. Glacier modelers can use these metrics to select the ~~input~~best possible velocity maps ~~based on these metrics in order~~ to derive physical quantities (such as strain rate) with minimal error propagation. When a velocity map has a $\delta_{x'y'}$ much larger than the suggested value, one can select an appropriate smoothing level for the velocity map and recalculate $\delta_{x'y'}$ until it reaches the suggested value. ~~For the velocity map~~Finally, we recommend that data producers calculate these metrics (with the help of the GLAFT package) and include in ~~each map metadata (with the help of the GLAFT package) so that users can determine if the product suits their needs or if a customized~~the metadata associated with each velocity product. This will enable users to assess product quality and determine if customized velocity maps are required for their applications.

To estimate the uncertainty of ice flow velocity, metric 1 (δ_u or δ_v) seems to be a plausible option and has been used in many studies (see Section 2.1). However, on-ice velocities likely have a different noise distribution than off-ice velocities, and the use of metric 1 as the flow uncertainty will be sub-optimal. Since metric 2 ($\delta_{x'y'}$) describes the spatial variability of the flow velocity, it can potentially offer an alternative uncertainty estimator. While the latter is one of the future goals of this project, at this time, we suggest that users should treat metric 1 as a very conservative image-wide uncertainty of the ice flow velocity.

Finally, the strategy outlined here is based on our analysis using optical images for one glacier. We expect that these metrics will also work for SAR feature tracking and different glacier settings, but additional care might be necessary. For example, SAR images typically have different range and azimuth resolutions, which could result in a significant difference between δ_u and δ_v. Also, it can be difficult to calculate both metrics over an ice sheet where there is no static terrain and limited differential velocity within a single scene. We will continue to address these issues in future GLAFT applications.

4.2 Open-source tools for computing quality metrics

The open-source ~~Python-based~~ GLAcier Feature Tracking testkit (GLAFT; Zheng et al., 2023) Python package accompanying this manuscript can be used to compute and evaluate these metrics and associated thresholds for arbitrary input velocity map

data. GLAFT contains modules for deriving and visualizing the two metrics from velocity maps generated by most feature-tracking tools. GLAFT is available on Ghub (Sperhac et al., 2021, https://theghub.org/resources/glaft) for cloud access and can be installed locally via PyPI, Python's official third-party package repository and manager (https://pypi.org/project/glaft). The GLAFT source code, Notebook examples, and documentation are hosted on Github (https://github.com/whyjz/GLAFT), with Binder-ready Jupyter Book pages (Project Jupyter et al., 2018; Executable Books Community, 2020) at https://whyjz.github.io/GLAFT/ as the supplemental material of this paper.

5 Conclusions

With the release of GLAFT and the strategy outlined in Table 2 to assess glacier velocity products, we anticipate that the Earth and Environmental Science community can quickly take advantage of the findings of this study. Our work sets up the first open-source benchmarking procedure for future large-scale intercomparison exercises (such as Boncori et al., 2018) that comprise multiple image sources and various feature-tracking workflows. ~~and even different use cases (e.g., sand dune mapping or earthquake displacement)~~With proper adjustments for the physics-based metrics, these methods can be applied to study different physical processes, such as dune migration or fault displacement. ~~Furthermore, for studies and policies related to~~The GLAFT enables the cryospheric sciences and natural hazards ~~and sea level rise, the GLAFT will help to assess the quality of~~communities to leverage the rich glacier velocity ~~maps already at hand~~data now available, whether they are sourced from public archives or ~~made through custom processes.~~prepared using one of the excellent open-source feature-tracking packages featured in this study.

Code and data availability. All the processing scripts, documentation, and other supplemental material (including Tables S1–S4 and Figures S1–S28) are available as Jupyter Book pages at https://whyjz.github.io/GLAFT/ (last access: 10 July 2023). The same content is also provided as a supplementary PDF file. The raw content of the Jupyter Book pages is hosted in the Github repository "whyjz/GLAFT" (https://github.com/whyjz/GLAFT, last access: 10 July 2023) and ~~corresponding Zenodo archive~~is archived by Zenodo (https://doi.org/10.5281/zenodo.7527956). The ~~GLAFT repository is rendered as~~ Jupyter Book pages are Binder-ready for full reproducibility. ~~Users can launch the MyBinder server by clicking the "launch binder" button in the repository readme or the rocket button in the executable Jupyter Book pages.~~ The original Level-1 Landsat 8 and Sentinel-2 images are available from USGS Earth Explorer (https://earthexplorer.usgs.gov/). The ITS_LIVE glacier velocity data set is available at https://its-live.jpl.nasa.gov/. The clipped source images, derived velocity maps, and other data used or generated by this study are hosted on the Open Science Framework (OSF, https://doi.org/10.17605/OSF.IO/HE7YR).

The GLAFT Python package is available on PyPI (pip installation; https://pypi.org/project/glaft) and Ghub (https://theghub.org/resources/glaft), and its source code is hosted on Github (https://github.com/whyjz/GLAFT; https://doi.org/10.5281/zenodo.7527956). Relevant documentation and cloud-executable demos are on its Github pages (https://whyjz.github.io/GLAFT/).

Author contributions. W.Z. conceived the presented idea. W.Z., S.B., M.V.W.D.V., W.K., and D.S. designed the study. L.C. and C.D. installed and maintained the Kaskawulsh GNSS stations. W.K. and L.C. collected and processed the in-situ GNSS data. W.Z., S.B., and M.V.W.D.V.

processed and analyzed the glacier velocity maps. R.J.-I. deployed and optimized the GLAFT tool on Ghub for cloud access. F.P. secured the JMTE funding and helped realize the cloud-based, fully reproducible analysis presented in this study as supplemental materials. All authors
435   contributed to the writing and editing of the paper.

Competing interests.   The authors declare no competing interests.

Acknowledgements.   We thank Dr. Leigh Stearns and Dr. Brent Minchew for their insightful discussion and code-sharing practice. Also, a huge appreciation to the Ghub team for making GLAFT available on the platform. Whyjay Zheng was supported by the Jupyter Meets the Earth (JMTE) program, an NSF EarthCube funded project (grants 1928406 and 1928374). Shashank Bhushan was supported by a NASA
440   FINESST award (80NSSC19K1338). David Shean was supported by a NASA HiMAT-2 award (80NSSC20K1595). Luke Copland, Christine Dow and Will Kochtitzky thank the Natural Sciences and Engineering Research Council of Canada, Canada Foundation for Innovation, Ontario Research Fund, Northern Scientific Training Program, University of Ottawa and Polar Continental Shelf Program for funds to purchase and service the GNSS stations. Fieldwork for this project was conducted on Kluane First Nation Traditional Territory, and we thank them and Parks Canada for permission to work there.

References

Abe, T. and Furuya, M.: Winter speed-up of quiescent surge-type glaciers in Yukon, Canada, The Cryosphere, 9, 1183–1190, https://doi.org/10.5194/tc-9-1183-2015, 2015.

Ahn, Y. and Howat, I. M.: Efficient Automated Glacier Surface Velocity Measurement From Repeat Images Using Multi-Image/Multichip and Null Exclusion Feature Tracking, IEEE Transactions on Geoscience and Remote Sensing, 49, 2838–2846, https://doi.org/10.1109/TGRS.2011.2114891, 2011.

Altena, B. and Kääb, A.: Ensemble matching of repeat satellite images applied to measure fast-changing ice flow, verified with mountain climber trajectories on Khumbu icefall, Mount Everest, Journal of Glaciology, 66, 905–915, https://doi.org/10.1017/jog.2020.66, 2020.

Altena, B., Scambos, T., Fahnestock, M., and Kääb, A.: Extracting recent short-term glacier velocity evolution over southern Alaska and the Yukon from a large collection of Landsat data, The Cryosphere, 13, 795–814, https://doi.org/10.5194/tc-13-795-2019, 2019.

Altena, B., Kääb, A., and Wouters, B.: Correlation dispersion as a measure to better estimate uncertainty in remotely sensed glacier displacements, The Cryosphere, 16, 2285–2300, https://doi.org/10.5194/tc-16-2285-2022, 2022.

Argyriou, V. and Vlachos, T.: Performance study of gradient correlation for sub-pixel motion estimation in the frequency domain, IEE Proceedings - Vision, Image, and Signal Processing, 152, 107, https://doi.org/10.1049/ip-vis:20051073, 2005.

Armstrong, W. H., Anderson, R. S., Allen, J., and Rajaram, H.: Modeling the WorldView-derived seasonal velocity evolution of Kennicott Glacier, Alaska, Journal of Glaciology, 62, 763–777, https://doi.org/10.1017/jog.2016.66, 2016.

Baker, S. and Matthews, I.: Lucas-Kanade 20 Years On: A Unifying Framework, International Journal of Computer Vision, 56, 221–255, https://doi.org/10.1023/B:VISI.0000011205.11775.fd, 2004.

Beyer, R. A., Alexandrov, O., and McMichael, S.: The Ames Stereo Pipeline: NASA's Open Source Software for Deriving and Processing Terrain Data, Earth and Space Science, 5, 537–548, https://doi.org/10.1029/2018EA000409, 2018.

Bindschadler, R. A. and Scambos, T. A.: Satellite-Image-Derived Velocity Field of an Antarctic Ice Stream, Science, 252, 242–246, https://doi.org/10.1126/science.252.5003.242, 1991.

Boncori, J. P. M., Andersen, M. L., Dall, J., Kusk, A., Kamstra, M., Andersen, S. B., Bechor, N., Bevan, S., Bignami, C., Gourmelen, N., Joughin, I., Jung, H.-S., Luckman, A., Mouginot, J., Neelmeijer, J., Rignot, E., Scharrer, K., Nagler, T., Scheuchl, B., and Strozzi, T.: Intercomparison and Validation of SAR-Based Ice Velocity Measurement Techniques within the Greenland Ice Sheet CCI Project, Remote Sensing, 10, 929, https://doi.org/10.3390/rs10060929, 2018.

Bradski, G.: The OpenCV Library, Dr. Dobb's Journal of Software Tools, 2000.

Brencher, G., Handwerger, A. L., and Munroe, J. S.: InSAR-based characterization of rock glacier movement in the Uinta Mountains, Utah, USA, The Cryosphere, 15, 4823–4844, https://doi.org/10.5194/tc-15-4823-2021, 2021.

Broxton, M. J., Nefian, A. V., Moratto, Z., Kim, T., Lundy, M., and Segal, A. V.: 3D Lunar Terrain Reconstruction from Apollo Images, in: Advances in Visual Computing, edited by Bebis, G., Boyle, R., Parvin, B., Koracin, D., Kuno, Y., Wang, J., Wang, J.-X., Wang, J., Pajarola, R., Lindstrom, P., Hinkenjann, A., Encarnação, M. L., Silva, C. T., and Coming, D., pp. 710–719, Springer Berlin Heidelberg, Berlin, Heidelberg, 2009.

Burgess, E. W., Larsen, C. F., and Forster, R. R.: Summer melt regulates winter glacier flow speeds throughout Alaska, Geophysical Research Letters, 40, 6160–6164, https://doi.org/10.1002/2013GL058228, 2013.

Clarke, G. K.: A Short and Somewhat Personal History of Yukon Glacier Studies in the Twentieth Century, ARCTIC, 67, 1, https://doi.org/10.14430/arctic4355, 2014.

Clarke, G. K. C., Schmok, J. P., Ommanney, C. S. L., and Collins, S. G.: Characteristics of surge-type glaciers, Journal of Geophysical Research: Solid Earth, 91, 7165–7180, https://doi.org/10.1029/JB091iB07p07165, 1986.

Cuffey, K. and Paterson, W. S. B.: The Physics of Glaciers, Elsevier Inc., 4e edn., 2010.

485 Dehecq, A., Gourmelen, N., and Trouve, E.: Deriving large-scale glacier velocities from a complete satellite archive: Application to the Pamir-Karakoram-Himalaya, Remote Sensing of Environment, 162, 55–66, https://doi.org/10.1016/j.rse.2015.01.031, 2015.

Evans, S. G., Tutubalina, O. V., Drobyshev, V. N., Chernomorets, S. S., McDougall, S., Petrakov, D. A., and Hungr, O.: Catastrophic detachment and high-velocity long-runout flow of Kolka Glacier, Caucasus Mountains, Russia in 2002, Geomorphology, 105, 314–321, https://doi.org/10.1016/j.geomorph.2008.10.008, 2009.

490 Executable Books Community: Jupyter Book (v0.10), https://doi.org/10.5281/zenodo.4539666, 2020.

Fahnestock, M., Scambos, T., Moon, T., Gardner, A., Haran, T., and Klinger, M.: Rapid large-area mapping of ice flow using Landsat 8, Remote Sensing of Environment, 185, 84–94, https://doi.org/10.1016/j.rse.2015.11.023, 2016.

Foy, N., Copland, L., Zdanowicz, C., Demuth, M., and Hopkinson, C.: Recent volume and area changes of Kaskawulsh Glacier, Yukon, Canada, Journal of Glaciology, 57, 515–525, https://doi.org/10.3189/002214311796905596, 2011.

495 Friedl, P., Seehaus, T., and Braun, M.: Global time series and temporal mosaics of glacier surface velocities derived from Sentinel-1 data, Earth System Science Data, 13, 4653–4675, https://doi.org/10.5194/essd-13-4653-2021, 2021.

Gardner, A. S., Fahnestock, M. A., and Scambos, T. A.: ITS_LIVE Regional Glacier and Ice Sheet Surface Velocities, https://doi.org/10.5067/6II6VW8LLWJ7, 2019.

Heid, T. and Kääb, A.: Evaluation of existing image matching methods for deriving glacier surface displacements globally from optical
500 satellite imagery, Remote Sensing of Environment, 118, 339–355, https://doi.org/10.1016/j.rse.2011.11.024, 2012.

Henderson, D. J. and Parmeter, C. F.: Normal reference bandwidths for the general order, multivariate kernel density derivative estimator, Statistics & Probability Letters, 82, 2198–2205, https://doi.org/10.1016/j.spl.2012.07.020, 2012.

Holdsworth, G.: Primary Transverse Crevasses, Journal of Glaciology, 8, 107–129, https://doi.org/10.3189/S0022143000020797, 1969.

Holland, D. M., Thomas, R. H., de Young, B., Ribergaard, M. H., and Lyberth, B.: Acceleration of Jakobshavn Isbræ triggered by warm
505 subsurface ocean waters, Nature Geoscience, 1, 659–664, https://doi.org/10.1038/ngeo316, 2008.

Kääb, A., Winsvold, S., Altena, B., Nuth, C., Nagler, T., and Wuite, J.: Glacier Remote Sensing Using Sentinel-2. Part I: Radiometric and Geometric Performance, and Application to Ice Velocity, Remote Sensing, 8, 598, https://doi.org/10.3390/rs8070598, 2016.

Lei, Y., Gardner, A., and Agram, P.: Autonomous Repeat Image Feature Tracking (autoRIFT) and Its Application for Tracking Ice Displacement, Remote Sensing, 13, 749, https://doi.org/10.3390/rs13040749, 2021.

510 Lei, Y., Gardner, A. S., and Agram, P.: Processing methodology for the ITS_LIVE Sentinel-1 ice velocity products, Earth System Science Data, 14, 5111–5137, https://doi.org/10.5194/essd-14-5111-2022, 2022.

Main, B., Copland, L., Smeda, B., Kochtitzky, W., Samsonov, S., Dudley, J., Skidmore, M., Dow, C., Van Wychen, W., Medrzycka, D., Higgs, E., and Mingo, L.: Terminus change of Kaskawulsh Glacier, Yukon, under a warming climate: retreat, thinning, slowdown and modified proglacial lake geometry, Journal of Glaciology, pp. 1–17, https://doi.org/10.1017/jog.2022.114, 2022.

515 Millan, R., Mouginot, J., Rabatel, A., Jeong, S., Cusicanqui, D., Derkacheva, A., and Chekki, M.: Mapping surface flow velocity of glaciers at regional scale using a multiple sensors approach, Remote Sensing, 11, 1–21, https://doi.org/10.3390/rs11212498, 2019.

Millan, R., Mouginot, J., Rabatel, A., and Morlighem, M.: Ice velocity and thickness of the world's glaciers, Nature Geoscience, 15, 124–129, https://doi.org/10.1038/s41561-021-00885-z, 2022.

Moon, T., Joughin, I., Smith, B., and Howat, I.: 21st-century evolution of Greenland outlet glacier velocities, Science, 336, 576–578, https://doi.org/10.1126/science.1219985, 2012.

Mouginot, J., Rignot, E., Bjørk, A. A., van den Broeke, M., Millan, R., Morlighem, M., Noël, B., Scheuchl, B., and Wood, M.: Forty-six years of Greenland Ice Sheet mass balance from 1972 to 2018, Proceedings of the National Academy of Sciences, 116, 9239–9244, https://doi.org/10.1073/pnas.1904242116, 2019.

Nefian, A. V., Husmann, K., Broxton, M., To, V., Lundy, M., and Hancher, M. D.: A bayesian formulation for sub-pixel re-finement in stereo orbital imagery, in: 2009 16th IEEE International Conference on Image Processing (ICIP), pp. 2361–2364, https://doi.org/10.1109/ICIP.2009.5413749, 2009.

Paul, F., Bolch, T., Briggs, K., Kääb, A., McMillan, M., McNabb, R., Nagler, T., Nuth, C., Rastner, P., Strozzi, T., and Wuite, J.: Error sources and guidelines for quality assessment of glacier area, elevation change, and velocity products derived from satellite data in the Glaciers_cci project, Remote Sensing of Environment, 203, 256–275, https://doi.org/10.1016/j.rse.2017.08.038, 2017.

Project Jupyter, Bussonnier, M., Forde, J., Freeman, J., Granger, B., Head, T., Holdgraf, C., Kelley, K., Nalvarte, G., Osheroff, A., Pacer, M., Panda, Y., Perez, F., Ragan-Kelley, B., and Willing, C.: Binder 2.0 - Reproducible, Interactive, Sharable Environments for Science at Scale, in: The 17th Python in Science Conference, https://doi.org/10.25080/Majora-4af1f417-011, 2018.

Redpath, T., Sirguey, P., Fitzsimons, S., and Kääb, A.: Accuracy assessment for mapping glacier flow velocity and detecting flow dynamics from ASTER satellite imagery: Tasman Glacier, New Zealand, Remote Sensing of Environment, 133, 90–101, https://doi.org/10.1016/j.rse.2013.02.008, 2013.

RGI Consortium: Randolph Glacier Inventory - A Dataset of Global Glacier Outlines, Version 6, https://doi.org/10.7265/4m1f-gd79, 2017.

Rosen, P. A., Hensley, S., Peltzer, G., and Simons, M.: Updated repeat orbit interferometry package released, Eos, Transactions American Geophysical Union, 85, 47, https://doi.org/10.1029/2004EO050004, 2004.

Rosen, P. A., Gurrola, E. M., Franco Sacco, G., and Zebker, H. A.: The InSAR Scientific Computing Environment, Proceedings of the 9th European Conference on Synthetic Aperture Radar, pp. 730–733, 2012.

Sciacchitano, A.: Uncertainty quantification in particle image velocimetry, Measurement Science and Technology, 30, 092 001, https://doi.org/10.1088/1361-6501/ab1db8, 2019.

Shangguan, D., Li, D., Ding, Y., Liu, J., Anjum, M. N., Li, Y., and Guo, W.: Determining the Events in a Glacial Disaster Chain at Badswat Glacier in the Karakoram Range Using Remote Sensing, Remote Sensing, 13, 1165, https://doi.org/10.3390/rs13061165, 2021.

Shean, D. and Bhushan, S.: vmap: Velocity map generation using the NASA Ames Stereo Pipeline (ASP) image correlator, https://doi.org/10.5281/zenodo.7730146, 2023.

Shepherd, A., Ivins, E., Rignot, E., Smith, B., van den Broeke, M., Velicogna, I., Whitehouse, P., Briggs, K., Joughin, I., Krinner, G., Nowicki, S., Payne, T., Scambos, T., Schlegel, N., A, G., Agosta, C., Ahlstrøm, A., Babonis, G., Barletta, V. R., Bjørk, A. A., Blazquez, A., Bonin, J., Colgan, W., Csatho, B., Cullather, R., Engdahl, M. E., Felikson, D., Fettweis, X., Forsberg, R., Hogg, A. E., Gallee, H., Gardner, A., Gilbert, L., Gourmelen, N., Groh, A., Gunter, B., Hanna, E., Harig, C., Helm, V., Horvath, A., Horwath, M., Khan, S., Kjeldsen, K. K., Konrad, H., Langen, P. L., Lecavalier, B., Loomis, B., Luthcke, S., McMillan, M., Melini, D., Mernild, S., Mohajerani, Y., Moore, P., Mottram, R., Mouginot, J., Moyano, G., Muir, A., Nagler, T., Nield, G., Nilsson, J., Noël, B., Otosaka, I., Pattle, M. E., Peltier, W. R., Pie, N., Rietbroek, R., Rott, H., Sandberg Sørensen, L., Sasgen, I., Save, H., Scheuchl, B., Schrama, E., Schröder, L., Seo, K. W., Simonsen, S. B., Slater, T., Spada, G., Sutterley, T., Talpe, M., Tarasov, L., van de Berg, W. J., van der Wal, W., van Wessem, M., Vishwakarma, B. D., Wiese, D., Wilton, D., Wagner, T., Wouters, B., and Wuite, J.: Mass balance of the Greenland Ice Sheet from 1992 to 2018, Nature, 579, 233–239, https://doi.org/10.1038/s41586-019-1855-2, 2020.

Shimizu, M. and Okutomi, M.: Precise sub-pixel estimation on area-based matching, in: Proceedings Eighth IEEE International Conference on Computer Vision. ICCV 2001, vol. 1, pp. 90–97, IEEE Comput. Soc, https://doi.org/10.1109/ICCV.2001.937503, 2001.

560 Shugar, D. H., Clague, J. J., Best, J. L., Schoof, C., Willis, M. J., Copland, L., and Roe, G. H.: River piracy and drainage basin reorganization led by climate-driven glacier retreat, Nature Geoscience, 10, 370–375, https://doi.org/10.1038/ngeo2932, 2017.

Shugar, D. H., Jacquemart, M., Shean, D., Bhushan, S., Upadhyay, K., Sattar, A., Schwanghart, W., McBride, S., de Vries, M. V. W., Mergili, M., Emmer, A., Deschamps-Berger, C., McDonnell, M., Bhambri, R., Allen, S., Berthier, E., Carrivick, J. L., Clague, J. J., Dokukin, M., Dunning, S. A., Frey, H., Gascoin, S., Haritashya, U. K., Huggel, C., Kääb, A., Kargel, J. S., Kavanaugh, J. L., Lacroix, P., Petley, D., Rupper, S., Azam, M. F., Cook, S. J., Dimri, A. P., Eriksson, M., Farinotti, D., Fiddes, J., Gnyawali, K. R., Harrison, S., Jha, M., Koppes,

565 M., Kumar, A., Leinss, S., Majeed, U., Mal, S., Muhuri, A., Noetzli, J., Paul, F., Rashid, I., Sain, K., Steiner, J., Ugalde, F., Watson, C. S., and Westoby, M. J.: A massive rock and ice avalanche caused the 2021 disaster at Chamoli, Indian Himalaya, Science, 373, 300–306, https://doi.org/10.1126/science.abh4455, 2021.

Silverman, B. W.: Density estimation for statistics and data analysis, Chapman and Hall, London, 1986.

Sperhac, J. M., Poinar, K., Jones-Ivey, R., Briner, J., Csatho, B., Nowicki, S., Simon, E., Larour, E., Quinn, J., and Patra, A.:

570 GHub : Building a glaciology gateway to unify a community, Concurrency and Computation: Practice and Experience, 33, 1–14, https://doi.org/10.1002/cpe.6130, 2021.

Stein, A., Huertas, A., and Matthies, L.: Attenuating stereo pixel-locking via affine window adaptation, in: Proceedings 2006 IEEE International Conference on Robotics and Automation, 2006. ICRA 2006., May, pp. 914–921, IEEE, https://doi.org/10.1109/ROBOT.2006.1641826, 2006.

575 Strozzi, T., Luckman, A., Murray, T., Wegmüller, U., and Werner, C. L.: Glacier motion estimation using SAR offset-tracking procedures, IEEE Transactions on Geoscience and Remote Sensing, 40, 2384–2391, https://doi.org/10.1109/TGRS.2002.805079, 2002.

Strozzi, T., Paul, F., Wiesmann, A., Schellenberger, T., and Kääb, A.: Circum-arctic changes in the flow of glaciers and ice caps from satellite SAR data between the 1990s and 2017, Remote Sensing, 9, 947, https://doi.org/10.3390/rs9090947, 2017.

Sundal, A., Shepherd, A., van den Broeke, M., Van Angelen, J., Gourmelen, N., and Park, J.: Controls on short-term variations in Greenland

580 glacier dynamics, Journal of Glaciology, 59, 883–892, https://doi.org/10.3189/2013JoG13J019, 2013.

Thomson, L. I. and Copland, L.: Multi-decadal reduction in glacier velocities and mechanisms driving deceleration at polythermal White Glacier, Arctic Canada, Journal of Glaciology, 63, 450–463, https://doi.org/10.1017/jog.2017.3, 2017.

Van Wychen, W., Copland, L., Jiskoot, H., Gray, L., Sharp, M., and Burgess, D.: Surface Velocities of Glaciers in Western Canada from Speckle-Tracking of ALOS PALSAR and RADARSAT-2 data, Canadian Journal of Remote Sensing, 44, 57–66,

585 https://doi.org/10.1080/07038992.2018.1433529, 2018.

Van Wyk de Vries, M. and Wickert, A. D.: Glacier Image Velocimetry: an open-source toolbox for easy and rapid calculation of high-resolution glacier velocity fields, The Cryosphere, 15, 2115–2132, https://doi.org/10.5194/tc-15-2115-2021, 2021.

Van Wyk de Vries, M., Bhushan, S., Jacquemart, M., Deschamps-Berger, C., Berthier, E., Gascoin, S., Shean, D. E., Shugar, D. H., and Kääb, A.: Pre-collapse motion of the February 2021 Chamoli rock–ice avalanche, Indian Himalaya, Natural Hazards and Earth System Sciences,

590 22, 3309–3327, https://doi.org/10.5194/nhess-22-3309-2022, 2022.

Van Wyk de Vries, M., Carchipulla-Morales, D., Wickert, A. D., and Minaya, V. G.: Glacier thickness and ice volume of the Northern Andes, Scientific Data, 9, 342, https://doi.org/10.1038/s41597-022-01446-8, 2022.

Van Wyk de Vries, M., Wickert, A. D., MacGregor, K. R., Rada, C., and Willis, M. J.: Atypical landslide induces speedup, advance, and long-term slowdown of a tidewater glacier, Geology, 50, 806–811, https://doi.org/10.1130/G49854.1, 2022.

595   Waechter, A., Copland, L., and Herdes, E.: Modern glacier velocities across the Icefield Ranges, St Elias Mountains, and variability at
        selected glaciers from 1959 to 2012, Journal of Glaciology, 61, 624–634, https://doi.org/10.3189/2015JoG14J147, 2015.

Willis, M. J., Melkonian, A. K., Pritchard, M. E., and Ramage, J. M.: Ice loss rates at the Northern Patagonian Icefield derived using a decade
        of satellite remote sensing, Remote Sensing of Environment, 117, 184–198, https://doi.org/10.1016/j.rse.2011.09.017, 2012.

Zheng, W.: Glacier geometry and flow speed determine how Arctic marine-terminating glaciers respond to lubricated beds, The Cryosphere,
600   16, 1431–1445, https://doi.org/10.5194/tc-16-1431-2022, 2022.

Zheng, W., Pritchard, M. E., Willis, M. J., and Stearns, L. A.: The possible transition from glacial surge to ice stream on Vavilov Ice Cap,
        Geophysical Research Letters, 46, 13 892–13 902, https://doi.org/10.1029/2019GL084948, 2019.

Zheng, W., Durkin, W. J., Melkonian, A. K., and Pritchard, M. E.: Cryosphere And Remote Sensing Toolkit (CARST) v2.0.0a1,
        https://doi.org/10.5281/zenodo.4592619, 2021.

605   Zheng, W., Bhushan, S., and Sundell, E.: GLAFT 0.2.0, https://doi.org/10.5281/zenodo.7527956, 2023.